

Effect of Heat-Treatment of Manganese Oxide Deposited on Stainless Steel 316L Current Collector Surface towards Carbon Based Supercapacitor Performance

B.N.M. Dolah, M. Deraman , M. Suleman, M.A.R. Othman, M.R.M. Jasni, N.S.M. Nor*

School of Applied Physics, Faculty of Science and Technology, Universiti Kebangsaan Malaysia, 43600 Bangi, Selangor, Malaysia

*E-mail: madra@ukm.edu.my, mderaman113@gmail.com

Received: 11 November 2016 / *Accepted:* 13 January 2017 / *Published:* 12 February 2017

Manganese oxide was deposited on the surface of stainless steel (SS) foil current collector (CC) using a simple immersion method followed by heat-treatment at three different temperatures (70, 200 and 400 °C) for 3 h. The CC deposited with manganese oxide without and with heat treatment were used in symmetrical supercapacitor cells using highly porous activated carbon electrodes and LiCl electrolyte. The heat-treatment changes the structure (from amorphous to crystalline phase) and surface morphology of manganese oxide deposited on the CC surface as evidenced by X-ray diffraction and field emission scanning electron microscopy studies. The electrochemical impedance spectroscopy, cyclic voltammetry and galvanic charge-discharge characterization results of the supercapacitor cells demonstrate that the heat-treatment temperature of 70 °C results in a maximum increase of ~70 % in specific capacitance, ~140 % in specific power and ~280 % in specific energy compared to the cell using CC deposited with manganese oxide at room temperature. Further, a 10-fold decrement in response time (from ~ 14 to ~ 1.4 s) is achieved for a heat-treatment at 70 °C which implies a ten times faster delivery of energy. These results show the superiority of CC deposited with manganese oxide heat-treated at 70 °C over the manganese oxide deposited at other temperatures.

Keywords: Wet chemical deposition, Activated carbon; Supercapacitors; Manganese oxide; Electrochemical properties.

1. INTRODUCTION

Electrochemical supercapacitors are energy storage devices which are capable of delivering higher energy densities than conventional capacitors and higher power densities with longer cycle life than batteries [1]. These advantages make them appealing as backup power sources, starting power for

fuel cells and hybrid power sources for many other applications [1,2]. The typical assembly of supercapacitors, in general, comprise of metal current collectors, active electrodes, electrolyte and separator. Depending on the types of electrodes and charge storage mechanism, the supercapacitors can be classified into three categories: (i) non-faradaic electric double layer capacitors (EDLCs) resulting from the accumulation of charges at the high surface area porous carbon electrode-electrolyte interface [3,4], (ii) faradaic pseudo-capacitors resulting from the fast and reversible redox reactions of electrochemically active electrode materials [5,6] and (iii) hybrid capacitor based on these two mechanisms [7]. The commonly used active electrode materials for pseudo-capacitor cells are conducting polymers (polypyrrole, polyaniline, etc.) and metal oxides (manganese oxide, ruthenium oxide, nickel oxide, cobalt oxide, vanadium oxide, etc.) [8]. Manganese oxide, due to its natural abundance, low toxicity, low cost, etc., has been proposed to be a better choice as electrode materials for supercapacitor applications [9–17].

Approach of using activated carbon (AC), carbon nanotube (CNT), graphene, carbon nano spheres, carbon aerogel etc., together with MnO_2 as electrode materials has been widely investigated [18]. The purpose of this approach is to utilize simultaneously the double layer capacitance from highly porous carbon materials and pseudo-capacitance from MnO_2 , an electroactive material, having the second highest capacitance after ruthenium oxide and being cheaper and environmental friendly. The main advantages of carbon materials are their higher electronic conductivity and internal surface area. The common methods to accomplish such an approach are by preparing composite electrodes such as MnO_2 -AC [18,19], MnO_2 -carbon nanocomposites [20,21], MnO_2 -nanoporous carbon [22], MnO_2 -porous carbon microsphere [23], MnO_2 -carbon nanoparticles [24], MnO_2 -ordered mesoporous carbon [25], MnO_2 -carbon xerogel [26], MnO_2 -CNT [27–31], MnO_2 -graphene [32–37], etc. These composites are commonly prepared by direct mixing of MnO_2 with carbon materials using binder [38], chemical precipitation [19] and electro-deposition [32] of MnO_2 on carbon materials. Another method that is similar to the above approach is based on designing of hybrid supercapacitor configuration, wherein carbon electrode is used as an anode and MnO_2 deposited on metal current collector (CC) such as stainless steel (SS) [9], nickel [39], indium-tin oxide (ITO) coated glass slides [40] etc., is used as cathode material. It has been reported that the specific capacitance values achieved by these approaches fall within the range of 111-940 F g^{-1} [1,5,10,18,19,40,41], where the values of specific capacitance recorded are highly dependent on the method of electrode preparation.

In the present paper, our method involves the deposition of MnO_2 on SS 316L CC by wet chemical dipping method using KMnO_4 as MnO_2 precursor followed by post-heat treatment. In order to produce high quality of MnO_2 deposited layer and to find the best heating condition, the heat-treatment was conducted over a few values of heat-treatment temperature. In fabricating supercapacitor cells, these CCs were used to sandwich two binderless AC monolith electrodes separated by polymer film separator wetted with LiCl electrolyte. The deposited surface of CC was made in contact with the AC monolith electrodes. The AC monolith electrodes were prepared from biomass fibers using our previously published method employed for producing electrodes for supercapacitor applications [42–52].

The changes in the structure and surface morphology of manganese oxide deposited on the CC surface were investigated by X-ray diffraction (XRD) and field emission scanning electron microscopy

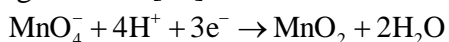
(FESEM) studies. The performance of the supercapacitor cells were evaluated by using electrochemical impedance spectroscopy (EIS), cyclic voltammetry (CV) and galvanostatic charge-discharge (GCD) techniques; and it was found that post heat-treatment of the manganese oxide conducted at an appropriate temperature (~ 70 °C) was very effective to enhance the performance of the supercapacitor cells in terms of capacitance, power and response time.

2. EXPERIMENTAL

2.1. Preparation of the electrode and deposition of manganese oxide

Fibers of oil palm empty fruit bunches (EFBs) were utilized as the precursor to produce activated carbon monoliths (ACM) following the procedure mentioned in our previous report [53]. First, the fibers were pre-carbonized (Furnace CTMSB46) at 280 °C, followed by milling (ball mill AC Motor BS 500-100), and sieving through a 106 μm mesh (Matest 24030 Brembate Sopra, BG) to obtain a powder of self-adhesive carbon grains (SACGs). The SACGs were then mixed with KOH (5 % by weight) and converted to green monoliths (GMs) using a press pelletizing machine (VISITEC 2009-Malaysia) inside a 20 mm-diameter mold. Carbonization of the GMs was performed under N_2 gas flow (1.5 l min^{-1}) inside a furnace (Vulcan Box Furnace 3-1750) to produce carbon monoliths (CMs) [53,54]. The CMs were then activated using CO_2 gas with flow rate of 1.0 l min^{-1} at a temperature of ~ 800 °C with a 3 h holding time [45,46]. The EFP produced were polished to 0.4 mm-thick and then washed with distilled water and dried.

Prior to the deposition process, the SS (grade 316L) current collector was cleaned using an ultrasonic bath with acetone, ethanol and de-ionized water for 10 min in each solution [43]. The solution for the growth of MnO on the surface of a SS current collector was prepared by mixing 80 ml of 0.2 M KMnO_4 in 20 ml of 2.5 M H_2SO_4 [2]. The CC was soaked in the solution for 60 min before washing with de-ionized water and then dried using N_2 at room temperature. The layer of amorphous MnO_2 was deposited by the reduction of Mn (VII) species from KMnO_4 solution according to the following reaction [12]:



Since no reducing agent was used, the free electrons are supposed to be supplied by the metallic SS current collector. The manganese oxide deposited SS current collectors were heat-treated at temperatures of 70 °C, 200 °C and 400 °C for 3 h in air and were labelled as SSMn70, SSMn200, SSMn400, respectively. For a comparison, reference sample SSMn00 (manganese oxide deposited stainless steel without heat treatment) was also prepared. The ACM electrodes, current collectors, egg-shell membrane separator and LiCl electrolyte (0.5 M) were used to fabricate asymmetric supercapacitor based on a previously reported method [55,56].

2.2 Physical and electrochemical characterization

The weights of the carbon electrodes were measured using a Mettler Toledo AB204 balance. Liquid nitrogen (77 K) adsorption-desorption isotherm experiments (Micromeretic ASAP 2010) were

conducted to characterize the porosity of the ACMs. The FESEM (Zeiss SUPRA 55VP) and energy dispersive X-ray analysis (EDAX) were used to study the surface morphology and elemental composition of the deposited manganese oxide on the surface of the SS current collectors that were heat-treated at various temperatures. The electrochemical performances of the fabricated supercapacitor cells were studied using the EIS in the frequency range of 1 MHz to 10 mHz, CV and GCD using a Solatron 1287 at a current density of 10 mA cm^{-2} . For the CV method, the CV responses were recorded over a scan rate increasing from 1 mV s^{-1} to 100 mV s^{-1} .

3. RESULTS AND DISCUSSION

3.1. Physical properties

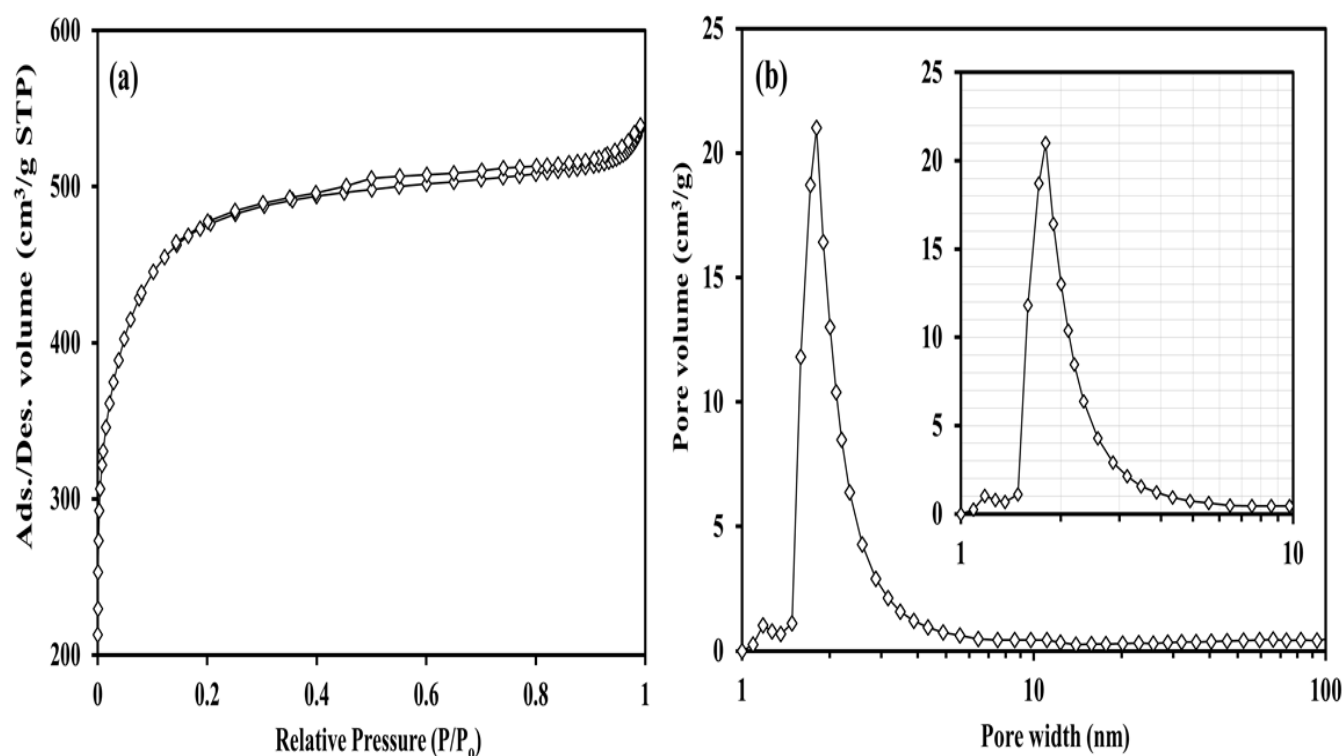


Figure 1. (a) Nitrogen adsorption-desorption isotherm data for the ACMs electrodes and (b) the corresponding pore size distribution.

Fig. 1(a and b) respectively present the nitrogen adsorption-desorption isotherm and pore size distribution curves for the ACM electrode materials used to fabricate supercapacitor cells. The nature of the isotherm corresponds to a combination of type-IV and type-I isotherms, an indicative of presence of porosity in the sample. It can be observed that initially the amount of gas adsorbed increases up to a pressure of ~ 0.1 which reveals that the electrode material possesses high internal surface area which has predominant contribution from micro-porosity. Further, a moderate increase in volume of adsorbed nitrogen gas beyond $\sim P/P_0 = 0.1$ and the presence of the hysteresis loop with a

sharp closure implies the availability of meso-pores. The presence of a much more widely distributed and heterogeneous micro-porosity in the electrodes was shown by the linear change in the adsorption quantity with increasing pressure [46]. At higher pressures, a ‘tail’ can be clearly observed, which is explained by the large number of pores in the ACM electrodes. Quantitative information about the porosity can be determined from the standard procedure by analyzing the nitrogen-adsorption isotherm data [57]. The values of the BET surface area (S_{BET}), micro-pore surface area (S_{mic}), meso-pore surface area (S_{meso}), meso-pore volume (V_{meso}), micro-pore volume (V_{mic}) and average pore diameter (D_p), determined using standard procedures and assisted by the instrument software, were $1592 \text{ m}^2 \text{ g}^{-1}$, $936 \text{ m}^2 \text{ g}^{-1}$, $656 \text{ m}^2 \text{ g}^{-1}$, $0.5 \text{ cm}^3 \text{ g}^{-1}$, $0.2 \text{ cm}^3 \text{ g}^{-1}$ and 2.1 nm , respectively. These values are typical for porous carbon electrodes [58].

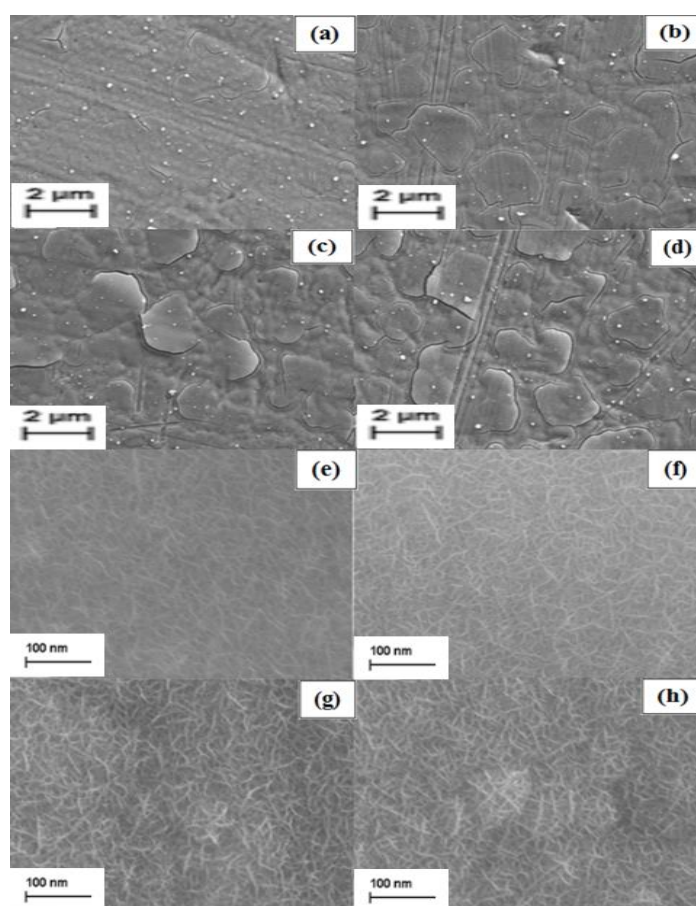


Figure 2. FESEM micrographs of (a) SSMn, (b) SSMn70, (c) SSMn200 and (d) SSMn400 (low magnification); and (e) SSMn, (f) SSMn70, (g) SSMn200 and (h) SSMn400 (high magnification).

In order to see the effect of heat-treatment over the surface morphology of manganese oxide deposited on SS current collector the FESEM micro-graphs were recorded. The FESEM images of SSMn00, SSMn70, SSMn200 and SSMn400 surfaces are shown in Fig. 2(i) (a to d) (low magnification) and Fig. 2(ii) (a to d) (high magnification). A comparison of the surface morphologies

of these figures shows the presence of the manganese oxide nanoparticles deposited on the surface of the SS current collectors. The manganese oxide nanoparticles layers appear to be evenly distributed throughout the surface of the current collectors; minor cracks appear after the heat treatment at a temperature of 70 °C, and severe cracks appear for higher heat treatment temperatures. The layer cracking can be attributed to drying shrinkage due to the release of water [1,59]. At higher magnification (100,000 X), as shown in Fig. 2(ii) (a to d), it can be observed that the morphology of the deposited manganese oxide has a nanostructured and porous fibrous network. Further, as the temperature of the heat-treatment increases from 70 °C to 200 °C and 400 °C (Figs. 2 (ii) (b, c and d)) the fibrous nanoparticles of the manganese oxide seem to tangle with each other and form an agglomeration of fibrous particles [1]. We will see in the later sections that these modified features in the surface morphology of the heat-treated electrode samples manifest themselves in enhanced supercapacitor performance. The EDAX spectra for the surfaces of all the deposited current collectors with manganese were recorded and analyzed using FESEM. It was found that manganese oxide deposited on the surface can be observed in the EDAX spectra from the manganese deposited current collectors. These results can be observed from the comparison of the spectra of in Fig. 3(i and ii).

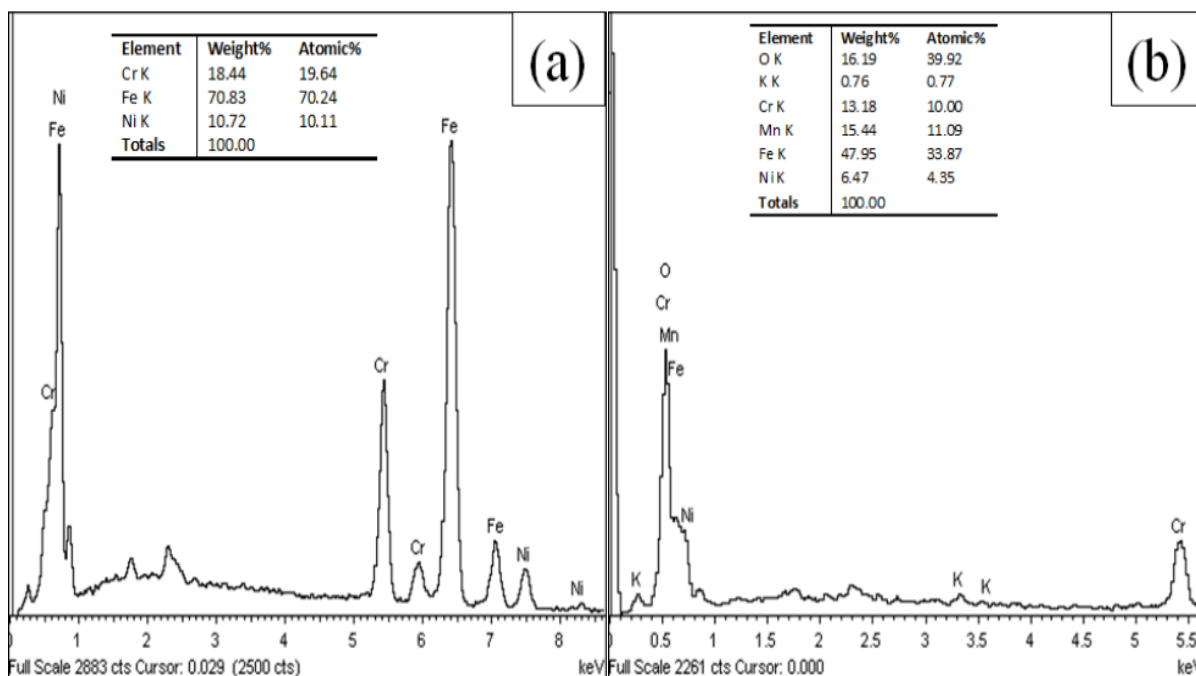


Figure 3. EDAX spectra of (a) SS current collector surface and (b) manganese oxides-SS current collector.

Fig. 4 shows the XRD patterns for SSMn00, SSMn70, SSMn200 and SSMn400 samples. It can be observed from the XRD pattern of SSMn00 (without heat-treatment) that there are two sharp peaks at $2\theta = 45.6^\circ$ and 50.7° which are the characteristic peaks of stainless steel and there are no peaks corresponding to manganese oxide which implies that the manganese oxide is in amorphous phase

[12,42]. However, with increase of temperature beyond 70 °C, a new peak $\sim 75^\circ$ appears and the intensity of the peaks 45.6° and 50.7° increases which indicates a transformation from amorphous manganese to the crystalline manganese oxide due to the release of water [1,60].

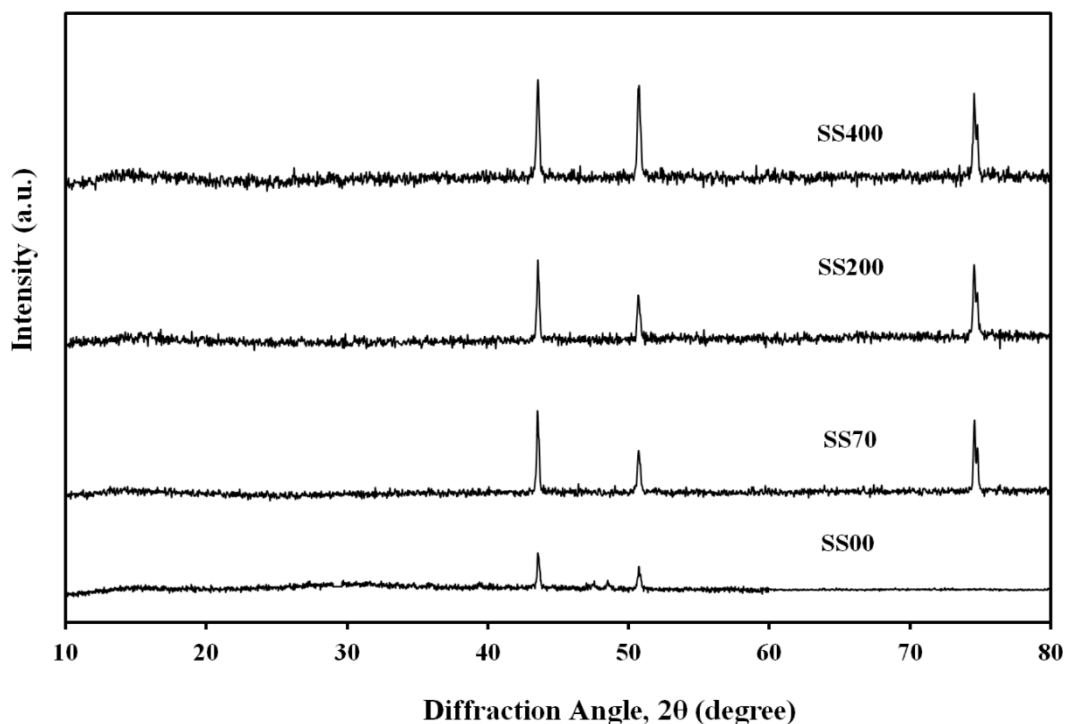


Figure 4. XRD patterns of (a) SSMn, (b) SSMn70, (c) SSMn200 and (d) SSMn400.

3.2. Electrochemical characterization

3.2.1 Electrochemical impedance spectroscopy

Fig. 5(a) presents the Nyquist plots of all the cells: Cell-00, Cell-70, Cell-200, and Cell-400 in the frequency range from 1 MHz to 10 mHz. Each cell shows a plot with a similar feature of the graph consisting of a semicircle, a Warburg impedance line and a steep rising line, respectively, in the high, intermediate and low frequency regions, and represents the resistive, resistive-capacitive and capacitive behavior of the cells in the respective domain of the frequency. However, the shapes of graphs differ from each other because of the effect of heat-treatment applied on MnO_2 . All the plots show typical shapes of EIS data curves of supercapacitors using MnO_2 , activated carbon, CNT and graphene electrodes [20–23,27,31,33,61–63], which are the resultant characteristics of the both capacitive components associated with the electric double layer phenomena and pseudo-capacitive components associated with Faradaic redox processes.

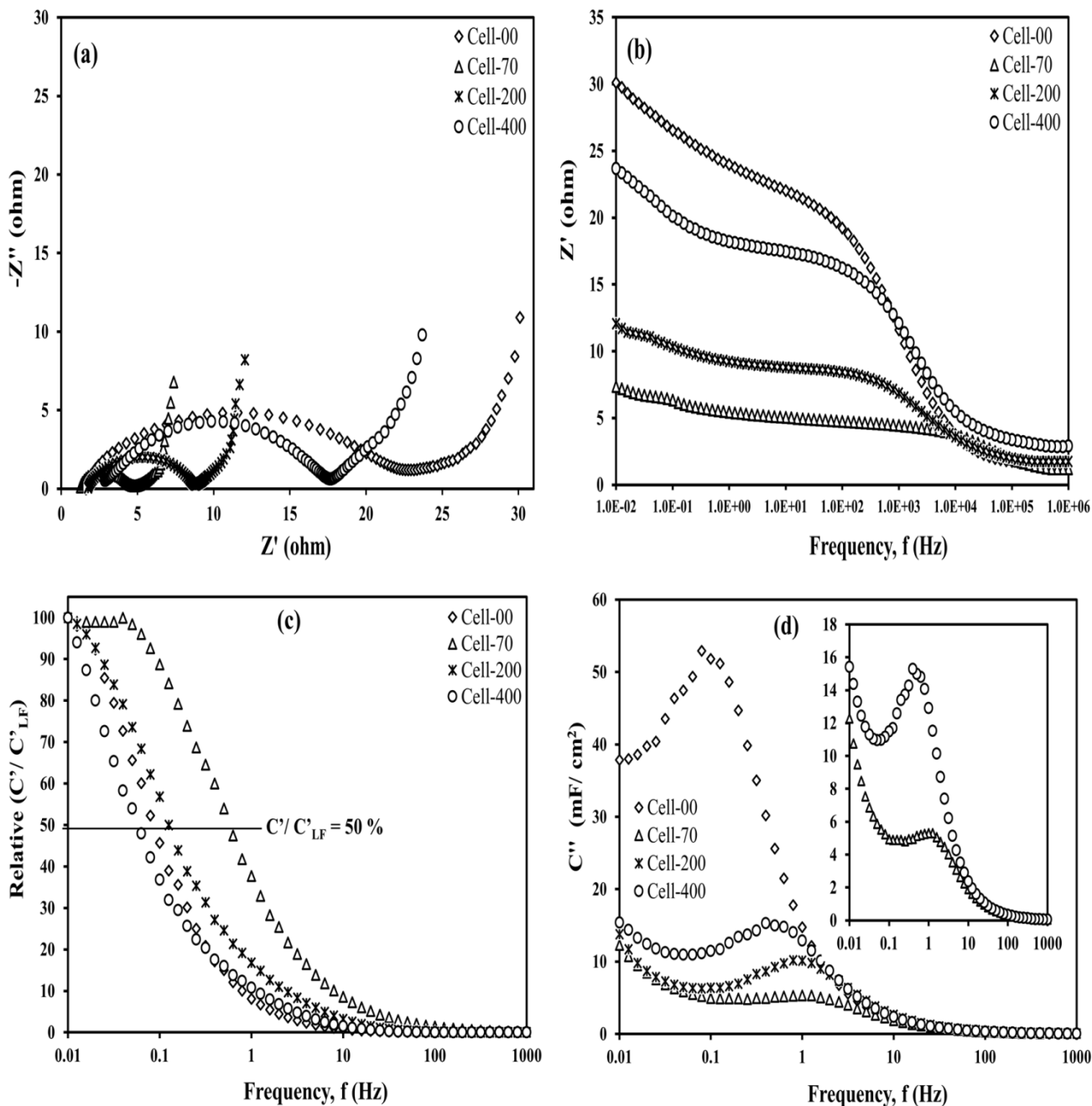
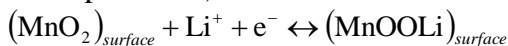


Figure 5. (a) Nyquist plots of all the cells over a frequency range of 10^{-1} to 10^6 Hz, (b) ESR as function of frequency, (c) Relative specific capacitance (C'/C'_{LF}) as a function of frequency, (d) Imaginary specific (area normalized) capacitance as a function of frequency.

The specific capacitance, C_{sp} of the cells were determined at 10 mHz (low frequency region) using the expression; $C_{sp} = 2 / (m \times \omega Z'')$, where $\omega = 2\pi f$ is angular frequency of applied signal, Z'' is the imaginary part of impedance and m is the mass of the electrode material used in the single electrode, and the results are listed in Table 1. The table shows that the Cell-70, Cell-200, and Cell-400 offer higher values of specific capacitance with respect to the Cell-00. This increase in capacitance can be accounted for the surplus pseudo-capacitance arising from the increase in electrical conductivity of MnO_2 and better interfacial contact of MnO_2 with carbon electrodes as result of enhanced crystallinity

(as observed from XRD patterns) and the surface roughness (as observed from FESEM images) of the MnO₂ layer used in the heat-treated samples/cells (Cell-70, Cell-200, and Cell-400) [64,65]. On the other hand, the as-prepared MnO₂ is poorly crystalline with high surface area and for this case the double layer capacitance is predominant [9,10,65]. Further, the low electronic conductivity of the poorly crystalline/amorphous MnO₂ decreases the charge transfer rate (and hence contribution from the pseudo-capacitance) in the redox reaction:



occurring primarily at the electrochemically active surface of the MnO₂ that involves surface adsorption or the intercalation/de-intercalation of Li⁺ cations [11–13,65].

Further, it can be observed from Table 1 that the C_{sp} values of the Cell-200 and Cell-400 are lower as compared to the Cell-70. This lowering in capacitance values with increase in temperature beyond 70 °C can be attributed to both the reduction in double layer capacitance (due to decrease in area of MnO₂ as the surface of the electrode specimen becomes denser) and pseudo-capacitance (due to reduced electronic conductivity as a result of increase in cracks/disintegration) [11,14,64,65]. Moreover, the decrease in effective surface area of MnO₂ in contact of carbon electrodes leads to relatively lower number of redox active sites for the adsorption of the Li⁺ ions and hence a relative lowering in capacitance values is observed for further increase in temperature beyond 70 °C [10–12,65]. This indicates that the heat-treatment can effectively change the electrochemical properties of the MnO₂ layer deposited on the SS current collectors. Similar significant changes in the electrochemical properties of the electrodes were observed when the MnO₂ electrodes were heat-treated at various temperatures: 200 – 400 °C [60], 70 – 400 °C [38], 50 – 600 °C [15] and 100 – 700 °C [1]. The common effects of heat-treatment of MnO₂ include changes in the microstructure, surface morphology, chemical state and crystal structure [10].

Table 1. Specific capacitance (C_{sp}) values evaluated from EIS, CV and GCD data for different supercapacitor cells.

Cells	C _{sp} (F g ⁻¹)		
	EIS	CV	GCD
Cell-00	58	60	56
Cell-70	100	98	96
Cell-200	77	85	82
Cell-400	65	80	75

The C_{sp} values presented in Table 1 are compared with those reported in the literature in Table 2 [1,2,9,18,20,22,25,27,32,34,38,39,61,62,66]. It can be observed from the Table 2 that except for a few configurations, most of the electrode configurations have higher, C_{sp} values than those of the supercapacitor cells under present investigation. The lower C_{sp} values can be due to the fact that when transporting from bulk of the electrolyte to the MnO₂ via carbon electrodes, the major fraction of Li⁺ ions are adsorbed by the carbon electrodes and only a small number of Li⁺ ions can manage to reach

the surface of MnO₂ due to diffusional limitations imposed majorly by the bottle neck micro-pores of the carbon electrodes. Therefore, the number of electroactive sites on the surface of MnO₂ contributing to the redox reactions is relatively less and hence a lesser contribution from the pseudo-capacitance is expected to the overall capacitance. However, we will see in the subsequent sections that a considerable decrease in Faradaic charge transfer resistance and that of electronic resistance is noteworthy due to the deposition of MnO₂ on the surface of high conducting SS current collector. This gives rise to the improved frequency response/rate capability of the supercapacitor cells.

Referring to the Fig. 5 (a), the first intersection point on the real axis by the high frequency RC semi-circle arc represents the combined resistance contributed by the electrolyte resistance, the ionic resistance of ions moving through the separator, the intrinsic resistance of the active electrode material, and the contact resistance at the interface of active material/current collector (R_s) and diameter of the arc represents the resistance mainly caused by the charge-transfer processes at the electrode/electrolyte interface (R_{ct}) and the double layer capacitance, (C_{dl}) [14,35,67]. Here, the Li⁺ cations participate in the redox processes during the charging/discharging [14]. The values of R_s and R_{ct} were determined from the EIS data in Fig. 5 (a) have been compared with the literatures (Table 3). This table shows that the R_s or ESR values of the cells under present investigation vary within the range from 1 to 2 Ω , and comparable to the value of bulk solution resistance of LiCl electrolyte [16]. R_s values offered by the heat-treated sample (Cell-70, Cell-200, and Cell-400) are lower than the as-prepared sample (Cell-00) and with an optimum improvement occurring for the heat-treatment at 70 °C. Further, it can also be noticed from this table that the R_{ct} values for the Cell-70, Cell-200, and Cell-400 are smaller and being a minimum for Cell-70 with respect to reference cell (Cell-00). In general, the variation in R_{ct} values is influenced by the current collector/active material interface contact resistance, electrode resistance, etc., [14,21,23,24,33,36,37,67,68].

Table 2. Specific capacitance values for MnO₂ and MnO₂ composite based supercapacitor cells.

Electrode configurations/compositions	C_{sp} (Fg ⁻¹)	Refs.
MnO ₂ -SS current collector (wet deposited) - binderless activated carbon electrodes: 70 °C, 200 °C, 400 °C)	96-100	Present study
MnO ₂ -graphite (Anodic deposition): As-deposited, 100 °C, 200 °C	179-214	[1]
MnO ₂ -SS current collector (Potentiodynamically deposited)	480	[9]
MnO ₂ -carbon nanocomposite	218	[20]
MnO ₂ (anode)-activated carbon (cathode)	300	[22]
MnO ₂ -Activated CNTs composite	201	[27]
MnO ₂ -activated CNT composite	184-250	[30]
MnO ₂ -ordered mesoporous carbon composite	440-640	[31]
MnO ₂ -graphene and MnO ₂ (Asymmetric)	328	[32]
MnO ₂ -graphene (anode)-activated carbon (cathode)	114	[34]
MnO ₂ -AB (acetylene black) (Symmetric composite): 70 °C, 200 °C, 400 °C	211-247	[38]
MnO ₂ - Ni current collector (Electrochemically deposited)	310	[39]
MnO ₂ -coated N ₂ -activated carbon-MWCT	63-312	[62]
MnO ₂ -activated carbon composite	70-150	[66]

As for our results, it is likely that the decrease in the R_{ct} values for heat-treated sample is dominantly related to the change in surface morphology (increased surface roughness) and increase in crystallinity of MnO_2 which respectively improves the MnO_2 layer adhesiveness to the current collector as well as the carbon electrodes; and conductivity of the electrodes [12,13,64,65]. Better contact of MnO_2 with CC facilitates electron conduction whereas increase in conductivity results in faster charge transfer rate [14].

The behavior of the R_{ct} values shown in Table 3 can be explained further by referring to the FESEM images in Fig. 2. It can be observed in this figure that the surface of the heat-treated MnO_2 (Cell-70) is relatively rough/uneven than untreated MnO_2 (Cell-00), which provides a better adherence to the particles of the carbon electrodes and hence reduces the interfacial contact resistance between MnO_2 and carbon electrodes. However, for higher heat-treatment temperature (Cell-200 and Cell-400) the surfaces are relatively rough than that of Cell-70, but more number of cracks/empty insulating pathways is generated due to the release of adsorbed water which leads to the reduction in area of MnO_2 . This reduction in area of the MnO_2 decreases the effective area of contact with current collectors as well as with carbon particles of the electrodes which in turn increases interfacial contact resistance between current collector and MnO_2 as well as between MnO_2 and carbon electrode.

Table 3. Electrical parameters evaluated from Nyquist and Bode Plots.

Cell/Electrode compositions	R_s (Ω)	R_{ct} (Ω)	τ_o (s)	Refs.
Cell-00	1.85	20.35	14.28	Present study
Cell-70	1.20	3.50	1.50	
Cell-200	1.65	6.00	8.33	
Cell-400	1.75	15.45	16.66	
MnO_2 (25–150 °C) heat treatment	0.50-5.04	0.10-0.70	0.06-0.23	[14]
MnO_2 -C (10-90)min	2.00	2.0-7.0	1.2-8.0	[21]
MnO_2 -(0 - 10%) carbon	0.20-0.420	0.5-1.5		[23]
MnO_2 -carbon nanoparticles	-	-	0.5	[24]
MnO_2 -GNR (0 - 23 %)	2.70-3.80	1.1-2.5	-	[33]
MnO_2 -rGO nanocomposite, GO and rGO	-	4.6-3.7	-	[36]
MnO_2 -NF, MnO_2 -G-gel-NF NF and G-gel-NF	-	4.2-9.6	-	[37]
MnO_2 -(30 - 50%) EG	152-216	0.566-0.798	-	[63]
MnO_2 -SWNT (before/after cycle)	2.71-2.48	0.97-1.24	-	[67]
MnO_2 -graphene	4.90	2.0-3.7	-	[68]

Fig. 5(b) is the plot of Z' values as a function of frequency, which can show the effect of heat treatment temperature of MnO_2 deposited layer on the equivalent series resistance (ESR) of the cells recorded over the all frequency range. It can be observed from the Fig. 5(b) that throughout the whole spectrum of frequency, the Cell-70 exhibits a behavior which is most close to the ideal one (represented by the line parallel to the real axis). At high frequencies ($f > 100$ Hz), the main resistances are due to electrolyte and the two electrodes, whereas in the intermediate frequency range ($1 \text{ Hz} < f <$

100 Hz), the predominant resistances are due to the transport/penetration of ions and the electric signal through the pores of electrodes [69]. Since the carbon electrodes and the electrolyte are same in all cases, therefore the lowest value of resistance for Cell-70 can be associated with the change in the properties (surface morphology, area, crystallinity etc., resulting in surplus pseudo-current) of the heat treated MnO₂. Finally, in the lower frequency range ($f < 1$ Hz) at a frequency of 0.01 Hz the Cell-70 offers an ESR of $\sim 6 \Omega$ which is substantially lower compared with that of as prepared Cell-00 ($\sim 30 \Omega$); and hence again confirming the improvement in the response time/frequency response caused by the heat-treatment.

For further analysis of the EIS data, it is convenient to refer the complex model of the capacitance, which assumes that the overall capacitance $C(\omega)$ can be split into two parts namely the real part, $C'(\omega)$ and the imaginary part, $C''(\omega)$, both being the functions of frequency [65,66]:

$$C(\omega) = C'(\omega) - jC''(\omega)$$

where $C'(\omega) = Z''(\omega) / \omega |Z(\omega)|^2$ and $C''(\omega) = -Z'(\omega) / \omega |Z(\omega)|^2$ such that $Z(\omega) = 1 / j\omega C(\omega)$, Z' = real impedance, and Z'' = imaginary impedance. These formula are used to determine the values of $C'(\omega)$ and $C''(\omega)$ from the EIS data for further analysis in the following paragraphs.

Fig. 5(c) displays the behavior of relative capacitance $C'(\omega)/C'(\omega)_{LF}$ decay as a function of increasing frequency for all the cells. This behavior can be explained by the complex model of the capacitance which proposes the 'rule' that the penetration depth inside pores of electrodes that can be reached by a.c. signal/ions is inversely proportional to the frequency of the applied a.c. signal [70,71]. In view of this rule one can explain for the significantly higher level of relative capacitance of the Cell-70 compared to other cells over a wide frequency range as seen in Fig. 5(c). For this cell, the better contact of MnO₂ with the interface: electrode/MnO₂/current collector (leading to the reduction in ESR and/or R_{ct} values facilitates the penetration of Li⁺ and Cl⁻ ions) into carbon electrodes and increases the number of Li⁺ ions reaching MnO₂ as a consequence of increased electroactive sites. The increase in conductivity of MnO₂ has also an added influence to promote better rate of redox reactions. Therefore, an equilibrium state resulting in the maximum/saturated capacitance is achieved for the Cell-70. However, such a condition does not occur in other cells, therefore, the relative capacitance curves for these do not show any plateau (equilibrium) feature even though in the very low frequency region.

From Fig. 5(c) one can estimate the highest operating frequency, f_{max} , which is defined as the frequency at which the capacitance drops to 50 % of its maximum value [72], and the values obtained are listed in Table 3. The Cell-70 presents the highest value of f_{max} compared to that of other cell. These results can be explained in terms of the temperature dependent growth of MnO₂ layer [12]. Our results show that the growth rate of MnO₂ can be accelerated at higher temperature (above 70 °C) which results in thicker MnO₂ layer leading to longer diffusion length and restricted transportation of the charge species. Therefore, higher f_{max} values or the rapid frequency response of the Cell-70 can be attributed to the relatively thin layer of along with the better contact with electrode and current collector. The value of f_{max} in the present study is comparable to those recently reported in the literature for polypyrrole derived activated carbons, aerosol-carbon particles, activated carbon and CNTs [72,73].

Fig. 5(d) shows the effect of heat treatment on the variation of $C''(\omega)$ against frequency. This figure shows that the heat-treatment causes a decrease in $C''(\omega)$ values and a shift in the $C''(\omega)$ peak

positions towards high frequency. From this figure, one can determine the time constant, τ_0 , as an important parameter that corresponds to the boundary between the resistive and capacitive behavior of the supercapacitors, which refers to the time required by the cells to deliver their stored energy [59]. The values of τ_0 for each Cell-00, Cell-70, Cell-200 and Cell-400 are determined from their respective peak position ($f = f_0$) in Fig. 5(d) by an equation $\tau_0 = 1/f_0$ and the results obtained for τ_0 and f_0 are as listed in Table 3. As can be seen in the table, the Cell-70 presents the lower value of τ_0 compared to other cells, indicating that this cell can deliver its stored energy faster than the other cells. It should be noted here that the τ_0 values in Table 3 are comparable to those reported for cells using MnO_2 [14] and MnO_2 -carbon composite electrodes [21,24].

3.2.2 Cyclic voltammetry

Fig. 6(a) presents the cyclic voltammograms for the Cell-00, Cell-70, Cell-200 and Cell-400 recorded at a scan rate of 1 mV s^{-1} over a potential window ranging from 0 to 1 V. The quasi-rectangular shape of the voltammograms of all the cells indicates near ideal capacitive behavior. The absence of redox peaks suggests that the MnO_2 in contact of carbon electrode is charged-discharged at pseudo-constant rate over the complete cyclic voltammetric cycles [23]. The pattern of the CV curves is similar to the typical symmetric voltammograms reported for composite electrodes consisting of MnO_2 and activated carbon [19,74], MnO_2 and carbon nanofibres [40], MnO_2 coated on graphite [2], MnO_2 and porous carbon meso-spheres [41], carbon supported MnO_2 [66], MnO_2 and ordered mesoporous carbon nanocomposite [25] etc. The uses of these carbon components are meant for increasing the electronic conductivity, mechanical strength and/or a source of electrostatic double layer capacitance [2,13,19,23,25,40,66,74].

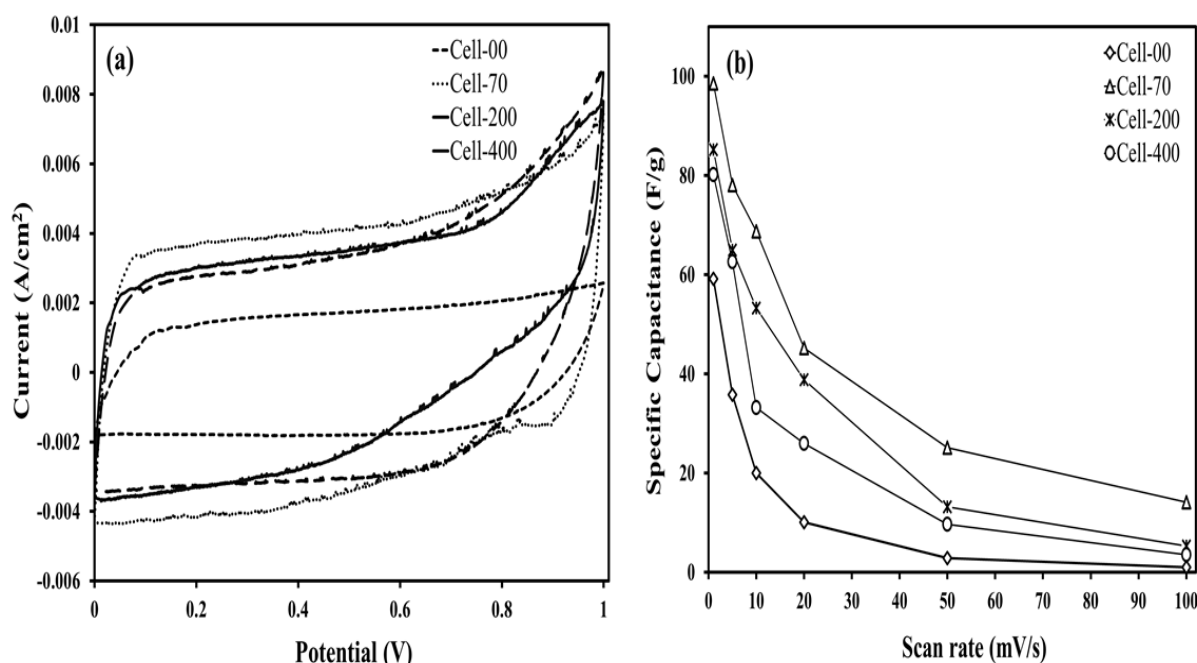


Figure 6. (a) CV profiles of all the cells at a scan rate of 1 mV s^{-1} , (b) Specific capacitance as a function of scan rates (from 1 mV s^{-1} to 100 mV s^{-1}).

The CV curves in Fig. 6(a) demonstrate that the Cell-70, Cell-200 and Cell-400 offer higher voltammetric current (and hence higher specific capacitance) and are closer to the rectangular shape as compared to the reference Cell-00. The specific capacitance of all the cells was calculated from the data in Fig. 6 (a) using the equation $C_{sp} = 2i/(sm)$, where i is the current, s is the scan rate, and m is the mass of the active material used for single electrode [43]. The results calculated from the CV curves at a scan rate of 1 mV s^{-1} are shown in Table 1. The change in the C_{sp} values is associated with the transformation from amorphous to the high electronic conducting crystalline phase of MnO_2 that occurred due to the heat-treatment, which in turn produces relatively high pseudo-current [13,65].

It is also noticeable in Table 1 that the Cell-200 and Cell-400 offer lower value of specific capacitance as compared to Cell-70 which can be accounted for the decrease in amount of hydrates and area of MnO_2 and hence reduced electrochemically active regions [14,65]. Further, the shape of CV profile of Cell-70 is very close to the rectangular like shape which indicates the improved accessibility of the Li^+ ions to the electrochemically active regions on the surface of MnO_2 in contact of the carbon electrodes and the fast Li^+ ion switching behavior across the electrolyte-carbon electrode interface and quick double layer formation in pores of the carbon electrodes.

The C_{sp} values over the scan rate of 1 to 100 mV s^{-1} are shown in Figs. 6 (b). It is noteworthy that the Cell-70, Cell-200 and Cell-400 exhibit higher value of specific capacitance over the entire range of scan rate and compared to Cell-00 for which only the $\sim 2\%$ capacitance is retained; the capacitance retention is improved to the maximum value of $\sim 15\%$ for Cell-70. Usually, such decrease in capacitance with increasing scan rates for the MnO_2 and MnO_2 composites with various carbons (AC, CNT, graphene etc.) is substantially higher as compared to the pristine carbon based electrodes which involve no redox reactions [2,4,19,23,25,40,66,74]. The retention/decay in the specific capacitance values in the present study is comparable to those observed over a typical range of scan rate for an asymmetric hybrid supercapacitor using composite electrodes based on carbon aerogel and manganese oxide [1,26,40,66].

The improvement in the capacitance retention for the Cell-70, Cell-200 and Cell-400 could be due to the following factors: (i) increase in electronic conductivity of MnO_2 , (ii) decrease in charge transfer resistance, R_{ct} , which represents either the kinetic resistance to ions transporting across the carbon electrode-electrolyte interface or intrinsic charge-transfer resistance in redox reactions occurring on the surface of MnO_2 and (iii) the improved interfacial (SS/MnO_2 and $\text{MnO}_2/\text{carbon}$ electrodes interfaces) contact.

Fig. 6(b) also shows the Cell-200 and Cell-400 have lower ER value of specific capacitance and lower capacitance retention as compared to Cell-70. These results could be due to the creation of more pronounced cracks/disintegration and decrease in amount of hydrates/area of MnO_2 in the Cell-200 and Cell-400 due to higher heat treatment temperature, which leads to reduced number of electroactive/hopping sites for Li^+ ions and pathways for electrons migrating across the SS/MnO_2 interface [11,14,23,25,40,64]. These results show that the annealing of manganese oxide conducted at an appropriate temperature may enhance the specific capacitance of the cell.

3.2.3 Galvanostatic charge-discharge

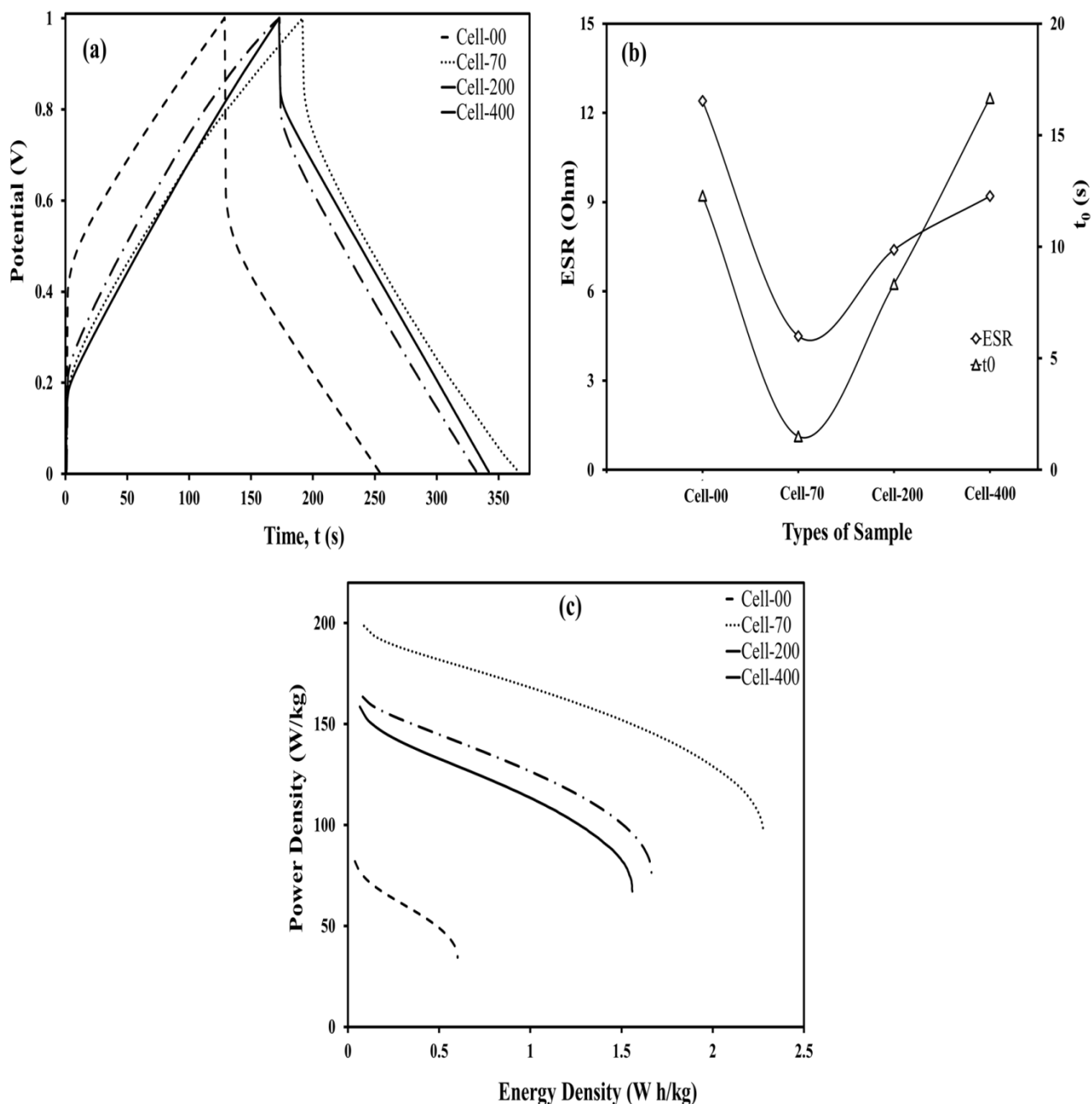


Figure 7. (a) Charge-discharge curves of all the cells at an applied constant current load of 1.0 mA cm^{-2} . (b) Equivalent series resistance (ESR) and response time (τ_0) as a function heat-treatment temperature and (c) Ragone plots for all the cells.

Fig. 7(a) shows the charge-discharge curves of the Cell-00, Cell-70, Cell-200 and Cell-400 at a constant current load of 1.0 mA cm^{-2} . Of all the curves, the GCD curve of Cell-70 shows the best charge-discharge behavior which is most close to the typical triangular curve for high performance supercapacitor, indicating an appropriate choice of heat-treatment temperature at $70 \text{ }^\circ\text{C}$ for MnO_2 deposited on the current collector. From the data in this figure, the values of discharge capacitance C_{sp}

for all the cells have been evaluated from the linear part of the discharge characteristics using the expression: $C_{sp} = 2i / m(\Delta V/\Delta t)$, where i is constant current, m is mass of the active material in the single electrode and $\Delta V/\Delta t$ is the slope of the discharge curve. The results are shown in Table 1, showing a good agreement with the C_{sp} values determined from the data of EIS and CV methods, which also indicate the highest C_{sp} value of the Cell-70.

It can be observed from the Fig. 7(a) that the heat-treatment influences the magnitude of the sudden voltage drop occurring at the beginning of the discharge curve. This voltage drop, also known as Ohmic drop, is related to the ESR by the equation $ESR = iR_{drop} / 2I$, where I discharge current and iR drop is electrical potential difference. The ESR of each cell has been evaluated from this voltage drop using this equation and the results are shown in Table 4. The ESR results in this table show the same trend as exhibited by the ESR results determined from EIS data, with minimum value of ESR observed for the Cell-70. Also, the ESR values in Table 4 show a well systematic correlation with the τ_0 values determined from the EIS data, as evidently shown in Fig. 7(b), where both parameters show minimum values for the Cell-70, confirming that this cell can deliver the highest performance of power delivery compared to the other cells.

The specific power (P) and specific energy (E) of the cells were calculated from the GCD curves in Fig. 7(a) using the equations $P = Vi / m$ and $E = Vit / m$, respectively, where V is the voltage (excluding the iR drop) that appears at the beginning of the discharge, i is the discharge current, t is time, and m is the mass of the electrode [47]. The effect of heat-treatment of MnO_2 on the P - E relation (Ragone plot) is shown in Fig. 7(c). All cells show a typical shape of P - E relation for carbon based supercapacitors but the level and the length of P - E curve of the cells differ from each other, depending on the heat-treatment temperature.

Table 4. Specific energy and specific power values evaluated from GCD data.

Cell/Electrode compositions	Aqueous Electrolyte	E_{max} (Whkg ⁻¹)	P_{max} (kW kg ⁻¹)	Refs.
Cell-00	LiCl	0.6	82	Present work
Cell-70	LiCl	2.3	199	
Cell-200	LiCl	1.7	163	
Cell-400	LiCl	1.6	159	
MnO ₂ - graphite (Anodic deposition)	LiCl	No report	No report	[2]
MnO ₂ -carbon spheres	Na ₂ SO ₄	-	13.5	[18]
MnO ₂ -CNT (Symmetric)	Na ₂ SO ₄	25.2	45.4	[28]
MnO ₂ - AC-MWCNT (Asymmetric)	Na ₂ SO ₄	51.1	0.1	[34]
MnO ₂ -Ni (Electrochemical deposition)	Na ₂ SO ₄	12.5	14.0	[39]
MnO ₂ -AC & AC (Asymmetric)	Na ₂ SO ₄	20.0	-	[66]

Specific power-energy relationship shows that the specific energy remains almost unchanged at low specific power and then gradually decreases before showing a relatively larger decrease in the region of higher specific power. The values of P_{max} and E_{max} are shown in Table 4. It can be seen that the heat-treatment results in substantial increase in both the P and E values, particularly for the Cell-

70, which shows the maximum increase compared to the Cell-00. It can, therefore, be inferred that an optimum heat-treatment temperature applied on MnO₂ during deposition on the current collector is a cause for substantial increase in the values of P , E and C_{sp} of the cell. The values of P_{max} and E_{max} shown in Table 4 are comparable to the recently reported values in the literature for supercapacitors using composite electrodes of manganese oxide and carbon based materials [22,28,32,34,38,75].

4. CONCLUSIONS

The performance of the heat-treated (70, 200 and 400 °C) manganese oxide layer deposited on the surface of stainless steel (SS) foil was compared with the as-prepared manganese oxide layer deposited on the surface of stainless steel (SS) foil at room temperature by fabricating the symmetrical supercapacitor cells using highly porous carbon electrodes prepared from fibers of oil palm empty fruit bunches and aqueous LiCl electrolyte. The changes in the structure and surface morphology of manganese oxide deposited on the SS surface caused by the heat-treatment influence the behaviour of MnO₂ in the interface: carbon electrode/MnO₂/CC and hence the performance of supercapacitor cells. A heat-treatment temperature of 70 °C results in a maximum increase of ~73 %, ~143 % and ~283 % in specific capacitance, specific power and specific energy, respectively, of the supercapacitor cell. Further, the Cell-70 (corresponding to the heat-treatment at 70 °C) offers the minimum value of time constant (~1.4 s). These results show the superiority of SS foil deposited with manganese oxide and heat-treated at an appropriate temperature (70 °C) over the manganese oxide deposited at other temperatures.

ACKNOWLEDGEMENTS

We acknowledge grants from the Ministry of Education (FRGS/1/2016/STG07/UKM/02/2), (FRGS/2/2013/ST05/UKM/01/1), National University of Malaysia (DIP-2014-027) and the support of CRIM (Centre for Research and Innovation Management). The authors also thank Mr. Saini Sain for help with laboratory work.

References

1. J. K. Chang, Y. L. Chen, W. T. Tsai, *J. Power Sources*, 135 (2004) 344.
2. C. C. C. Lin, H. W. W. Chen, *Electrochim. Acta*, 54 (2009) 3073.
3. M. Suleman, Y. Kumar, S. A. Hashmi, *Electrochim. Acta*, 182 (2015) 995.
4. E. Frackowiak, Q. Abbas, F. Beguin, *J. Energy. Chem.*, 22 (2013) 226.
5. S. Hassan, M. Suzuki, A. Abd El-Moneim, *American. J. Mater. Sci.*, 2 (2012) 11.
6. Suhasini, *J. Electroanal. Chem.*, 690 (2013) 13.
7. B. E. Conway, *Electrochemical Supercapacitors: Scientific Fundamentals and Technological Applications*, Kluwer Academic/ Plenum Publisher, New York, 1999.
8. G. Q. Q. Zhang, S. T. T. Zhang, *J. Appl. Electrochem.*, 39 (2009) 1033.
9. K. R. Prasad, N. Miura, *J. Power Sources*, 135 (2004) 354.
10. W. Wei, X. Cui, W. Chen, D. G. Ivey, *Chem. Soc. Rev.*, 40 (2011) 1697.
11. M. W. Xu, D. D. Zhao, S. J. Bao, H. L. Li, *J. Solid. State. Electrochem.*, 11 (2007) 1101.

12. J. Yan, E. Khoo, A. Sumboja, P. S. Lee, *ACS Nano*, 4 (2010) 4247.
13. M. Toupin, T. Brousse, D. Belanger, *Chem. Mater.*, 16 (2004) 3184.
14. S. E. Chun, S. I. Pyun, G. J. Lee, *Electrochim. Acta*, 51 (2006) 6479.
15. H. N. V. P. Ragupathy, N. Munichandraiah, *J. Electrochem. Soc.*, 155 (2008) A34.
16. S. L. Kuo, N. L. Wu, *J. Electrochem. Soc.*, 153 (2006) A1317.
17. M. Huang, F. Li, F. Dong, X. Zhang, L. Li, *J. Mater. Chem., A Mater. Energy Sustain.*, 3 (2015) 21380.
18. G. Z. Wu, X. Y. Guo, J. Q. Zhou, D. Zhao, Y. Gao, M.G. Li, F. Gao, *Ecs Solid State Lett.*, 1 (2012) M8.
19. X. Zhang, X. Sun, H. Zhang, D. Zhang, Y. Ma, *Mater. Chem. Phys.*, 137 (2012) 290.
20. Y. Peng, Z. Chen, J. Wen, Q. Xiao, D. Weng, S. He, H. Geng, W. Lu, *Nano Res*, 4 (2011) 216.
21. C. Yang, M. Zhou, Q. Xu, *Phys. Chem. Chem. Phys.*, 15 (2013) 19730.
22. T. Tomko, R. Rajagopalan, M. Lanagan, H.C. Foley, *J. Power Source*, 196 (2011) 2380.
23. M. Liu, L. Gan, W. Xiong, Z. Xu, D. Zhu, L. Chen, *J. Mater. Chem. A.*, 2 (2014) 2555.
24. L. Yuan, X. Lu, X. Xiao, T. Zhai, J. Dai, F. Zhang, B. Hu, X. Wang, L. Gong, J. Chen, C. Hu, Y. Tong, J. Zhou, Z. L. Wang, *ACS Nano*, 6 (2011) 656.
25. M. A. Kiani, H. Khani, N. Mohammadi, *J. Solid State Electrochem.*, 18 (2014) 1117.
26. F. Lufrano, P. Staiti, E. G. Calvo, E. J. J.Perez, J. A Menendez, A. Arenillas, *Int. J. Electrochem. Sci.*, 6 (2011) 596.
27. L. Li, Z. A. Hu, N. An, Y. Y. Yang, Z. M. Li, H. Y. Wu, *J. Phys. Chem. C.*, 118 (2014) 22865.
28. J. Yan, Z. Fan, T. Wei, J. Cheng, B. Shao, K. Wang, L. Song, M. Zhang, *J. Power Sources*, 194 (2009) 1202.
29. B. N. M. Dolah, M. A. R. Othman, M. Deraman, N. H. Basri, R. Farma, I. A. Talib, M. M. Ishak, *J. Phys. Conf. Ser.*, 431 (2013) 12015.
30. K. H. An, W. S. Kim, Y. S. Park, J. M. Moon, D. J. Bae, S. C. Lim, Y. S. Lee, Y. H. Lee, *Adv. Funtional Mater.*, 11 (2001) 387.
31. H. Huang, W. Zhang, Y. Fu, X. Wang, *Electrochim. Acta*, 152 (2014) 480.
32. Q. Cheng, J. Tang, J. Ma, H. Zhang, N. Shinya, L.C. Qin, *Carbon*, 49 (2011) 2917.
33. M. Liu, W. W. Tjiu, J. Pan, C. Zhang, W. Gao, T. Liu, *Nanoscale*, 6 (2014) 4233.
34. Z. Fan, J. Yan, T. Wei, L. Zhi, G. Ning, T. Li, F. Wei, *Adv. Funct. Mater.*, 21 (2011) 2366.
35. W. Yang, Z. Gao, J. Wang, B. Wang, Q. Liu, Z. Li, T. Mann, P. Yang, M. Zhang, L. Liu, *Electrochim. Acta*, 69 (2012) 112.
36. Y. Sun, Y. Cheng, K. He, A. Zhou, H. Duan, *RSC Adv.*, 5 (2015) 10178.
37. T. Zhai, F. Wang, M. Yu, S. Xie, C. Liang, C. Li, F. Xiao, R. Tang, Q. Wu, X. Lu, Y. Tong, *Nanoscale*, 5 (2013) 6790.
38. P. Staiti, F. Lufrano, *J. Power Sources*, 187 (2009) 284.
39. S. Devaraj, N. Munichandraiah, *Solid-State Lett*, 8 (2005) A373.
40. J. G. Wang, Y. Yang, Z.H. Huang, F. Kang, *Electrochim. Acta*, 56 (2011) 9240.
41. S. Kong, K. Cheng, Y. Gao, T. Ouyang, K. Ye, G. Wang, D. Cao, *J. Power Source*, 308 (2016) 141.
42. E. Taer, M. Deraman, I. A. Talib, A. A. Umar, M. Oyama, R. M. Yunus, *Curr. Appl. Phys.*, 10 (2010) 1071.
43. E. Taer, M. Deraman, I. A. Talib, S. A. Hashmi, A. A. Umar, *Electrochim. Acta*, 56 (2011) 10217.
44. A. Awitdrus, M. Deraman, I. A. Talib, R. Farma, R. Omar, M. M. Ishak, N. H. Basri, B. N. M. Dolah, *Adv. Mater. Res.*, 501 (2012) 13.
45. R. Farma, M. Deraman, A. Awitdrus, I. A. Talib, E. Taer, N. H. Basri, J. G. Manjunatha, M. M. Ishak, B. N. M. Dolah, S. A. Hashmi, *Bioresour. Technol.*, 132 (2013) 254.
46. R. Farma, M. Deraman, A. Awitdrus, I. A. Talib, R. Omar, J. G. Manjunatha, M. M. Ishak, N. H. Basri, B. N. M. Dolah, *Int. J. Electrochem. Sci.*, 8 (2013) 257.
47. B. N. M. Dolah, M. Deraman, M. A. R. Othman, R. Farma, E. Taer, Awitdrus, N. H. Basri, I. A.

- Talib, R. Omar, N. S. M. Nor, *Mater. Res. Bull.*, 60 (2014) 10.
48. N. S. M. Nor, M. Deraman, R. Omar, Awitdrus, R. Farma, N. H. Basri, B. N. M. Dolah, N. F. Mamat, B. Yatim, M. N. M. Daud, *Energy*, 79 (2015) 183.
49. M. R. M. Jasni, M. Deraman, E. Hamdan, N. E. S. Sazali, N. S. M. Nor, M. M. Ishak, N. H. Basri, R. Omar, M. A. R. Othman, R. Zulkifli, R. Daik, M. Suleman, *Mater. Sci. Forum.*, 846 (2016) 551.
50. M. R. M. Jasni, M. Deraman, M. Suleman, E. Hamdan, N. E. S. Sazali, N. S. M. Nor, S. A. Shamsudin, *AIP Conf. Proc.*, 1710 (2016) 30034.
51. S. Soltaninejad, R. Daik, M. Deraman, Y. C. Chin, N. S. M. Nor, N. E. S. Sazali, E. Hamdan, M. R. M. Jasni, M. M. Ishak, M. Noroozi, M. Suleman, *Int. J. Electrochem. Sci.*, 10 (2015) 10524.
52. R. Farma, M. Deraman, S. Soltaninejad, Awitdrus, E. Taer, M. M. Ishak, N. S. M. Nor, N. H. Basri, B. N. M. Dolah, N. K. Othman, M. A. R. Othman, R. Daik, M. Suleman, G. Hegde, *Electrochemistry*, 83 (2015) 1053.
53. M. Deraman, R. Omar, S. Zakaria, I. R. Mustapa, M. Talib, N. Alias, *J. Mater. Sci.*, 37 (2002) 3329.
54. M. Deraman, S. Zakaria, M. Husin, A. A. Aziz, R. Ramli, A. Mokhtar, M. N. M. Yusof, M. H. Sahri, *J. Mater. Sci. Lett.*, 18(1999) 249.
55. E. Taer, I. Iwantono S. T. Manik, R. Taslim, D. Dahlan, M. Deraman, *Adv. Mater. Res.*, 896 (2014) 179.
56. N. S. M. Nor, M. Deraman, R. Omar, E. Taer, R. Farma, N.H. Basri, B. N. M. Dolah, *AIP Conf. Proc.*, 1586 (2014) 68.
57. X. Li, W. Xing, S. Zhuo, J. Zhou, F. Li, S. Z. Qiao, G. Q. Lu, *Bioresour. Technol.*, 102 (2011) 1118.
58. B. Kishore, D. Shanmughasundaram, T. R. Penki, N. Munichandraiah, *J. Appl. Electrochem.*, 44 (2014) 903.
59. Q. Huang, X. Wang, J. Li, *Electrochim. Acta.*, 52 (2006) 1758.
60. C. K. Lin, K. H. Chuang, C. Y. Lin, C. Y. Tsay, C. Y. Chen, *Surf. Coatings Technol.*, 202 (2007) 1272.
61. J. M. Ko, K. M. Kim, *Mater. Chem. Phys.*, 114 (2009) 837.
62. K. Shi, I. Zhitomirsky, *ChemElectroChem.*, 2 (2015) 396.
63. H. R. Naderi, H. R. Mortaheb, A. Zolfaghari, *J. Electroanal. Chem.*, 719 (2014) 98.
64. S. Park, I. Nam, G. P. Kim, J. W. Han, J. Yi, *ACS Appl. Mater. Interfaces.*, 5 (2013) 9908.
65. M. Toupin, T. Brousse, D. Belanger, *Chem. Mater.*, 14 (2002) 3946.
66. I. Acznik, K. Lota, A. Sierczynska, G. Lota, *Int. J. Electrochem. Sci.*, 9 (2014) 2518.
67. X. Li, B. Wei, *Nano Energy*, 1 (2012) 479.
68. H. Gao, F. Xiao, C. B. Ching, H. Duan, *ACS Appl. Mater. Inter.*, 4 (2012) 2801.
69. P. L. Taberna, P. Simon, J.F. Fauvarque, *J. Electrochem. Soc.*, 150 (2003) A292.
70. Y. Z. Wei, B. Fang, S. Iwasa, M. Kumagai, *J. Power Sources*, 141 (2005) 386.
71. R. De. Levie, *Electrochim. Acta*, 8 (1963) 751.
72. L. Wei, M. Sevilla, A. B. Fuertes, R. Mokaya, G. Yushin, *Adv. Funct. Mater.*, 22 (2012) 827.
73. Z. Chen, D. Weng, H. Sohn, M. Cai, Y. Lu, *RSC Adv.*, 2 (2012) 1755.
74. M. S. Hong, S. H. Lee, S. W. Kim, *Electrochem. Solid-State Lett.*, 5 (2002) A227.
75. V. Khomenko, E. Raymundo. Piñero, F. Beguin, *J. Power Sources*, 153 (2006) 183.